

ADAPTIVE RELATIVE POSE ESTIMATION FRAMEWORK WITH DUAL NOISE TUNING FOR SAFE APPROACHING MANEUVERS

Batu Candan^{*} and Simone Servadio[†]

Accurate and robust relative pose estimation is crucial for enabling challenging Active Debris Removal (ADR) missions targeting tumbling derelict satellites such as ESA's ENVISAT. This work presents a complete pipeline integrating advanced computer vision techniques with adaptive nonlinear filtering to address this challenge. A Convolutional Neural Network (CNN), enhanced with image preprocessing, detects structural markers (corners) from chaser imagery, whose 2D coordinates are converted to 3D measurements using camera modeling. These measurements are fused within an Unscented Kalman Filter (UKF) framework, selected for its ability to handle nonlinear relative dynamics, to estimate the full relative pose. Key contributions include the integrated system architecture and a dual adaptive strategy within the UKF: dynamic tuning of the measurement noise covariance compensates for varying CNN measurement uncertainty, while adaptive tuning of the process noise covariance, utilizing measurement residual analysis, accounts for unmodeled dynamics or maneuvers online. This dual adaptation enhances robustness against both measurement imperfections and dynamic model uncertainties. The performance of the proposed adaptive integrated system is evaluated through high-fidelity simulations using a realistic ENVISAT model, comparing estimates against ground truth under various conditions, including measurement outages. This comprehensive approach offers an enhanced solution for robust onboard relative navigation, significantly advancing the capabilities required for safe proximity operations during ADR missions.

INTRODUCTION

The capability to estimate the relative pose of uncooperative targets, such as derelict satellites, is critical for enabling future ADR, on-orbit servicing, and space situational awareness missions. These scenarios are characterized by severe visibility challenges, unpredictable dynamics, and uncertain sensor performance, all of which make traditional, rigid estimation pipelines inadequate. In particular, ESA's ENVISAT has become a key benchmark target for ADR due to its large size, complex structure, and non-cooperative nature [1–3]. Moreover, it represents a risk for the sustainability of the LEO space environment [4, 5]. Recent advances in vision-based navigation and machine learning have dramatically improved object detection in space imagery [6–9]. CNNs and deep learning models enable the detection of structural markers on a spacecraft from camera images, even under challenging lighting and motion conditions [10–12]. However, these visual outputs still face significant uncertainty due to sensor limitations, jitter, and partial or complete occlusions [13]. Therefore, fusing these noisy, intermittent detections into a reliable navigation solution remains

^{*}PhD Student, Department of Aerospace Engineering, Iowa State University, IA 50011, USA. email: dukynuke@iastate.edu

[†]Assistant Professor, Department of Aerospace Engineering, Iowa State University, IA 50011, USA. email: servadio@iastate.edu

a central challenge. To address this, Kalman filtering and its nonlinear variants, particularly the UKF, have emerged as robust solutions for visual navigation [14–19]. Yet, traditional filters assume fixed noise models, which often do not reflect the real-world variability encountered during proximity operations [20–22]. This results in either over-conservative or overly confident estimations depending on operational conditions. While prior works have attempted to tune the process noise covariance matrix \mathbf{Q} adaptively, many approaches suffer from either computational complexity or limited scalability. Mamich et al. [23] propose a variational Bayesian approach to estimate \mathbf{Q} using a probabilistic inference framework, but this requires iterative updates of the evidence lower bound, posing a significant challenge for real-time systems. Similarly, Moghe et al. [24] explore dynamic \mathbf{Q} estimation in reinforcement learning settings, relying on sampling-based uncertainty propagation that increases computational burden with state dimension. Zanetti and D’Souza [25] analyze filter robustness under observability constraints and propose cautious tuning heuristics for \mathbf{Q} , but lack an adaptive mechanism that reacts online to system dynamics.

In contrast to existing approaches, this paper introduces a fully adaptive, dual-noise tuning framework for vision-based relative navigation, with particular emphasis on spacecraft proximity operations under uncertainty. Our main novelty lies in the joint online adaptation of both the process noise covariance matrix \mathbf{Q} and the measurement noise covariance matrix \mathbf{R} using real-time filter statistics, without requiring prior eclipse scheduling, tuning heuristics, or batch post-processing. The \mathbf{Q} adaptation leverages a forward–backward residual matrix, inspired by the Rauch–Tung–Striebel (RTS) smoother [26], to capture the mismatch between prior and propagated sigma points and to adjust process noise during unobservable or eclipse phases. Simultaneously, the \mathbf{R} tuning strategy employs a residual consistency filter that tracks innovation growth in real-time and injects per-marker correction factors through the Multiple Tuning Factor (MTF) diagonal matrix inspired by the author’s previous works and others [27–29]. This dual-adaptation architecture allows the filter to remain responsive to both system-driven and measurement-driven uncertainty, achieving consistent and bounded covariance behavior. To the best of our knowledge, this is the first integrated application of RTS-inspired \mathbf{Q} adaptation with innovation-based \mathbf{R} tuning for monocular vision-based relative navigation in space. The framework’s efficacy is demonstrated on high-fidelity simulations of ESA’s ENVISAT, where our approach outperforms previous work and variational Bayesian methods in both accuracy and computational efficiency, particularly under full measurement outages. The results from this effort advance the need for ADR [30] for the safety of the space environment and avoiding the predicted Kessler’s syndrome [31].

METHODOLOGY

This section details the proposed methodology, covering spacecraft dynamics (chaser and target), the ENVISAT simulation parameters, and the data preparation steps for image processing and estimation. Before starting with the methodology, it would be useful to discuss the assumptions made in this study. First, the mass and inertia properties of the target spacecraft, ENVISAT, are assumed to be known since we have required data from ESA’s technical handouts [32]. Second, the external disturbances that might affect the dynamic equations, such as gravitational perturbations, solar radiation pressure, atmospheric drag and etc., are ignored. Finally, it is assumed that the chaser spacecraft is equipped with a camera right behind the ENVISAT satellite in its orbit. Properties of the camera parameter and ways to simulate it are to be discussed in the following sections.

Dynamics

Absolute Chaser Motion: To model the chaser's motion, the following equations are used.

$$\ddot{\bar{r}} = \bar{r}\dot{\theta}^2 - \frac{\mu}{\bar{r}^2} \quad (1)$$

$$\ddot{\theta} = -2\frac{\dot{\bar{r}}\dot{\theta}}{\bar{r}} \quad (2)$$

They incorporate Earth's gravitational parameter (μ), the chaser's position vector with respect to Earth (\bar{r}), and its orbital true anomaly (θ).

Relative Translational Dynamics: The equations describing ENVISAT's relative translational motion are derived using the chaser's Local-Vertical-Local-Horizontal (LVLH) frame as the reference. Within this frame, the target's relative position is represented by the vector \mathbf{r}_r and its relative velocity by \mathbf{v}_r , as defined in:

$$\mathbf{r}_r = x\hat{\mathbf{i}} + y\hat{\mathbf{j}} + z\hat{\mathbf{k}} \quad (3)$$

$$\mathbf{v}_r = \dot{x}\hat{\mathbf{i}} + \dot{y}\hat{\mathbf{j}} + \dot{z}\hat{\mathbf{k}} \quad (4)$$

Here, x , y , and z are the elements of the position vector \mathbf{r}_r within the chaser frame, and $\hat{\mathbf{i}}$, $\hat{\mathbf{j}}$, and $\hat{\mathbf{k}}$ represent the unit vectors of the reference frame. So, the equations of relative motion of the target can be written in the following way:

$$\ddot{x} = 2\dot{\theta}\dot{y} + \ddot{\theta}y + \dot{\theta}^2x - \frac{\mu(\bar{r} + x)}{[(\bar{r} + x)^2 + y^2 + z^2]^{3/2}} + \frac{\mu}{\bar{r}^2} \quad (5)$$

$$\ddot{y} = -2\dot{\theta}\dot{x} - \ddot{\theta}x + \dot{\theta}^2y - \frac{\mu y}{[(\bar{r} + x)^2 + y^2 + z^2]^{3/2}} \quad (6)$$

$$\ddot{z} = -\frac{\mu z}{[(\bar{r} + x)^2 + y^2 + z^2]^{3/2}} \quad (7)$$

Rotational Dynamics: Let $\mathbf{\Gamma}$ be the rotation matrix defining the relative orientation between the chaser and target body-fixed frames. The relative angular velocity $\boldsymbol{\omega}_r$, expressed in the target's body frame, depends on the individual body-frame angular velocities of the chaser ($\boldsymbol{\omega}_c$) and the target ($\boldsymbol{\omega}_t$).

$$\boldsymbol{\omega}_r = \boldsymbol{\omega}_t - \mathbf{\Gamma}\boldsymbol{\omega}_c \quad (8)$$

$$\dot{\boldsymbol{\omega}}_r = \dot{\boldsymbol{\omega}}_t - \mathbf{\Gamma}\dot{\boldsymbol{\omega}}_c + \boldsymbol{\omega}_r \wedge \mathbf{\Gamma}\boldsymbol{\omega}_c \quad (9)$$

Modified Rodrigues Parameters (MRPs) are utilized to parametrize the relative attitude, represented by the rotation matrix $\mathbf{\Gamma}$. This choice leverages the MRPs' three-parameter and singularity-free nature for describing rotation. While quaternions (\mathbf{q} , including vector components q_1, q_2, q_3 , and scalar q_4) also represent orientation, MRPs are specifically utilized for the attitude parametrization in this work. The satellite's angular velocity vector is denoted $\boldsymbol{\omega}$, with components ω_x, ω_y , and ω_z .

$$\mathbf{q} = \begin{bmatrix} \bar{\mathbf{q}} \\ q_4 \end{bmatrix} \quad (10)$$

$$\bar{\mathbf{q}} = \begin{bmatrix} q_1 \\ q_2 \\ q_3 \end{bmatrix} = \hat{\mathbf{n}} \sin \frac{\phi}{2} \quad (11)$$

$$q_4 = \cos \frac{\phi}{2} \quad (12)$$

Defining $\hat{\mathbf{n}}$ as the unit vector along the rotation axis and ϕ as the corresponding rotation angle, the relationship connecting MRPs to quaternions is given as follows:

$$\mathbf{p} = \frac{\bar{\mathbf{q}}}{(1 + q_4)} = \hat{\mathbf{n}} \tan \frac{\phi}{4} \quad (13)$$

where \mathbf{p} is the three-dimensional MRP vector. The kinematic equation of motion can be derived from the target's relative angular velocity. This relationship yields the following expression for the time derivative of the MRPs:

$$\dot{\mathbf{p}} = \frac{1}{4} [(1 - \mathbf{p}^T \mathbf{p})\mathbf{I}_3 + 2\mathbf{p}\mathbf{p}^T + 2[\mathbf{p}\wedge]] \omega_{\mathbf{r}} \quad (14)$$

Note that \mathbf{I}_3 is a 3×3 identity matrix, and $[\mathbf{p}\wedge]$ identifies the 3×3 cross product matrix given as,

$$[\mathbf{p}\wedge] = \begin{bmatrix} 0 & -p_3 & p_2 \\ p_2 & 0 & -p_1 \\ -p_2 & p_1 & 0 \end{bmatrix} \quad (15)$$

Therefore, the rotation matrix Γ , which relates the body-fixed frame of the chaser to that of the target, can be expressed as follows:

$$\epsilon_1 = 4 \frac{1 - \mathbf{p}^T \mathbf{p}}{(1 + \mathbf{p}^T \mathbf{p})^2} \quad (16)$$

$$\epsilon_2 = 8 \frac{1}{(1 + \mathbf{p}^T \mathbf{p})^2} \quad (17)$$

$$\Gamma(\mathbf{p}) = \mathbf{I}_3 - \epsilon_1[\mathbf{p}\wedge] + \epsilon_2[\mathbf{p}\wedge]^2 \quad (18)$$

While the chaser's absolute rotational dynamics follow the torque-free Euler equations, the relative attitude dynamics are obtained by substituting kinematic relationships into the target's absolute Euler equations.

$$\mathbf{J}_{\mathbf{t}} \dot{\omega}_{\mathbf{r}} + \omega_{\mathbf{r}} \wedge \mathbf{J}_{\mathbf{t}} \omega_{\mathbf{r}} = \mathbf{M}_{app} - \mathbf{M}_g - \mathbf{M}_{ci} \quad (19)$$

Here, $\mathbf{J}_{\mathbf{t}}$ is the inertia matrix of the target spacecraft, while \mathbf{M}_{app} , \mathbf{M}_g , and \mathbf{M}_{ci} represent the apparent, gyroscopic, and chaser-inertial torques, respectively. The specific definitions for these terms are given as:

$$\mathbf{M}_{app} = \mathbf{J}_{\mathbf{t}} \omega_{\mathbf{r}} \wedge \Gamma \omega_{\mathbf{c}} \quad (20)$$

$$\mathbf{M}_g = \Gamma \omega_{\mathbf{c}} \wedge \mathbf{J}_{\mathbf{t}} \Gamma \omega_{\mathbf{c}} + \omega_{\mathbf{r}} \wedge \mathbf{J}_{\mathbf{t}} \omega_{\mathbf{c}} + \Gamma \omega_{\mathbf{c}} \wedge \mathbf{J}_{\mathbf{t}} \omega_{\mathbf{r}} \quad (21)$$

$$\mathbf{M}_{ci} = \mathbf{J}_{\mathbf{t}} \Gamma \dot{\omega}_{\mathbf{c}} \quad (22)$$

ENVISAT Satellite Simulation

To generate a realistic dataset reflecting space conditions, a simulation environment for the ENVISAT satellite was established and implemented using Python in the Blender environment *. This implementation includes a custom pinhole camera model and projection logic, also coded in Python, based on specified intrinsic parameters, leading to a defined camera matrix. The simulated 3D model, derived from ESA-provided data (mass, inertia, center of mass), focuses on the satellite's

*Blender 4.2.0 software is used in this work.

main rectangular body, specifically to assess corner detection algorithms [33]. The Blender simulation generates synthetic images by projecting the 3D model onto the image plane according to its time-varying state using the custom camera projection routines. A sequence of these generated images is demonstrated in Fig. 1. For each simulation step, key data were stored: the 12-component relative state vector (relative position, velocity, attitude represented by MRPs, and angular velocity) between the target and chaser, along with the true 2D pixel coordinates and depth values for each of the main corners as projected onto the image. These pixel locations and depths, calculated and saved by the Python script, serve as the precise ground truth for validating the corner detection algorithm. Note that until this point, in recent work, the camera simulation was conducted in a less realistic environment, while proper camera transformation, dynamic simulation, and rendering are implemented in Blender now [34]. Table 1 shows the camera parameters selected within this study which has been chosen similar to [35] as it is space enabled.



Figure 1. Simulated images of the ENVISAT satellite

Table 1. Camera intrinsic properties and simulation parameters

Parameter	Value
FoV (Field of view)	45°
f_x (Focal length in x-direction)	1280 (pxs)
f_y (Focal length in y-direction)	1280 (pxs)
c_x (Principal point x-coordinate)	640 (pxs)
c_y (Principal point y-coordinate)	640 (pxs)
Affine translation (std. dev.)	3 pixels (in both x and y)
Affine rotation (std. dev.)	1°
Additive Gaussian noise (std. dev.)	0.001 (normalized intensity)
Gaussian blur (sigma)	0.0 (disabled for this study)

CONVOLUTIONAL NEURAL NETWORK

Convolutional neural networks are deep learning models that can process grid-like data, such as images, automatically learning spatial feature hierarchies using convolutional, aggregating, and fully connected layers [36, 37]. Compared to other neural networks, CNNs generally require fewer trainable parameters, enhancing generalization and reducing overfitting. CNN architectures have evolved significantly in recent years, often increasing depth and employing specialized blocks to enhance performance in various applications [38]. In this project, the chosen neural network model is our lightweight CNN architecture design, named TinyCornerNET, developed specifically for structural marker detection on the ENVISAT satellite [35]. In contrast to more computationally demanding models such as L-CNN [39] or stacked hourglass networks, TinyCornerNET is tailored for simplicity and efficiency, making it ideal for deployment in real-time, resource-constrained spaceborne

environments. The network architecture comprises a sequence of convolutional layers with ReLU activations, followed by a final convolutional layer with a sigmoid activation to generate a marker likelihood map. The complete network structure is illustrated in Figure 2. The model is trained using a dataset of 100 randomly generated simulated images. The performance of TinyCornerNET with respect to other state-of-the-art networks is compared in [35].

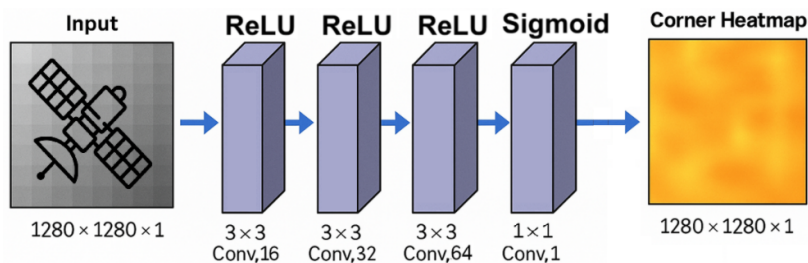


Figure 2. Overview of TinyCornerNET architecture.

Fig. 3 shows how effective the CNN algorithm is in detecting the corners of satellites in different orientations and illumination conditions within a simulated space environment. It also indicates that the marker association algorithm, which will be discussed in the next sections, works efficiently and is able to match the detected corners with the specific ground truth corners, which are labeled and known.



Figure 3. Preliminary results of CNN algorithm

Note that even though most of the corners can be projected into the image frame, some of them are not actually visible to the camera due to self-occlusion or obstruction by other satellite components. To ensure the realism and accuracy of the generated ground-truth data, we perform a visibility check using Blender’s raycasting functionality. Specifically, each corner’s 3D position is tested by casting a ray from the camera toward the marker to determine whether it is directly observable or blocked by other geometry in the scene. Only markers that pass this visibility test are included in the final dataset for projection and depth association. This approach improves the fidelity of our simulation by mimicking realistic line-of-sight constraints in space-borne imaging scenarios.

FILTERING

UKF is selected to estimate the relative pose of ENVISAT, due to its capacity to process nonlinear systems. Unlike the extended Kalman filter (EKF), which linearizes system dynamics, the UKF applies the unscented transformation to directly process nonlinearity. The approach propagates chosen sigma points cautiously to properly capture state uncertainty, while significantly retaining a linear measurement update suitable for onboard computational constraints [40].

The Filtering Algorithm

UKF sigma point weights are determined by parameters α, β, κ , which control the spread and scaling of the points. The scaling parameter λ is computed as:

$$\lambda = \alpha^2(L + \kappa) - L \quad (23)$$

where $L = 12$ is the state vector dimension. The weights for calculating the mean (W_m) and covariance (W_c) from the sigma points are:

$$W_m^{(0)} = \frac{\lambda}{L + \lambda} \quad (24)$$

$$W_c^{(0)} = \frac{\lambda}{L + \lambda} + (1 - \alpha^2 + \beta) \quad (25)$$

$$W_m^{(i)} = W_c^{(i)} = \frac{1}{2(L + \lambda)}, \quad i = 1, \dots, 2L \quad (26)$$

Prediction Step Sigma points $\chi_{k-1}^{(i)}$ are generated around the previous state estimate $\hat{\mathbf{x}}_{k-1}$ using the covariance \mathbf{P}_{k-1} :

$$\chi_{k-1}^{(i)} = \begin{cases} \hat{\mathbf{x}}_{k-1} & \text{for } i = 0 \\ \hat{\mathbf{x}}_{k-1} + (\sqrt{(L + \lambda)\mathbf{P}_{k-1}})_i & \text{for } i = 1, \dots, L \\ \hat{\mathbf{x}}_{k-1} - (\sqrt{(L + \lambda)\mathbf{P}_{k-1}})_{i-L} & \text{for } i = L + 1, \dots, 2L \end{cases} \quad (27)$$

These points are propagated through the nonlinear state transition function $f(\cdot)$ and the predicted state mean $\hat{\mathbf{x}}_{k|k-1}$ and covariance $\mathbf{P}_{k|k-1}$ are computed by weighted summation.

$$\chi_{k|k-1}^{(i)} = f(\chi_{k-1}^{(i)}, \mathbf{u}_{k-1}) \quad (28)$$

$$\hat{\mathbf{x}}_{k|k-1} = \sum_{i=0}^{2L} W_m^{(i)} \chi_{k|k-1}^{(i)} \quad (29)$$

$$\mathbf{P}_{k|k-1} = \sum_{i=0}^{2L} W_c^{(i)} \left(\chi_{k|k-1}^{(i)} - \hat{\mathbf{x}}_{k|k-1} \right) \left(\chi_{k|k-1}^{(i)} - \hat{\mathbf{x}}_{k|k-1} \right)^T + \mathbf{Q} \quad (30)$$

Update Step Propagated sigma points are transformed through the measurement function $h(\cdot)$:

$$\gamma_k^{(i)} = h(\chi_{k|k-1}^{(i)}) \quad (31)$$

The predicted measurement mean $\hat{\mathbf{z}}_k$ and measurement covariance \mathbf{S}_k are computed. Then, the cross-covariance \mathbf{T}_k and Kalman gain \mathbf{K}_k are calculated.

$$\hat{\mathbf{z}}_k = \sum_{i=0}^{2L} W_m^{(i)} \gamma_k^{(i)} \quad (32)$$

$$\mathbf{S}_k = \sum_{i=0}^{2L} W_c^{(i)} \left(\gamma_k^{(i)} - \hat{\mathbf{z}}_k \right) \left(\gamma_k^{(i)} - \hat{\mathbf{z}}_k \right)^T + \mathbf{R}_k \quad (33)$$

$$\mathbf{T}_k = \sum_{i=0}^{2L} W_c^{(i)} \left(\chi_{k|k-1}^{(i)} - \hat{\mathbf{x}}_{k|k-1} \right) \left(\gamma_k^{(i)} - \hat{\mathbf{z}}_k \right)^T \quad (34)$$

$$\mathbf{K}_k = \mathbf{T}_k \mathbf{S}_k^{-1} \quad (35)$$

Finally, the state estimate $\hat{\mathbf{x}}_k$ and covariance \mathbf{P}_k are updated using the actual measurement \mathbf{z}_k :

$$\hat{\mathbf{x}}_k = \hat{\mathbf{x}}_{k|k-1} + \mathbf{K}_k(\mathbf{z}_k - \hat{\mathbf{z}}_k) \quad (36)$$

$$\mathbf{P}_k = \mathbf{P}_{k|k-1} - \mathbf{K}_k \mathbf{S}_k \mathbf{K}_k^T \quad (37)$$

THE MEASUREMENT MODEL

The filter processes translational and rotational measurements but propagates the dynamics separately for efficiency. This treats the 12-element state vector as two independent 6-element vectors (translation/velocity and rotation/angular rate), integrated using a 4th-order Runge-Kutta method suitable for onboard use. The filter supports using all visible markers or a limited subset and can simulate measurement losses to test robustness. Performance evaluation involves comparing estimated states with high-accuracy simulated ground truth.

Markers Creation

For filters to precisely assess the target's attitude and correct the predicted values, precise measurements are necessary. The majority of filters used in space applications rely on image processing from cameras [41, 42]. In real-world situations, the image processing program is set up to recognize markers in every picture that is taken. After processing the camera image and determining the marker positions, the software sends this data to the filter. Given the need for quick image processing, choosing markers is a challenging issue that is impacted by the target's shape, volume, and color. Target corners are frequently chosen as markers using traditional corner detection algorithms such as the Förstner and Harris-Stephens [43–46] methods. It was determined to use the main body's corners as markers and monitor their positions over time in order to solve the ENVISAT relative pose estimation problem. Since each marker's location with respect to the center of mass is known, the marker placements can, therefore, provide useful information. The filter can determine the spacecraft's relative position and velocity as well as recreate its state by following the trajectory of these markers. The locations of these corners with respect to the center of mass are known, and they are chosen as the filter markers.

Camera Transformation and 3D Reconstruction from 2D Pixel Data

Converting the 2D-pixel coordinates detected by the CNN module into 3D spatial positions is necessary to accurately locate the satellite markers. This back-projection utilizes both intrinsic and extrinsic camera parameters based on a pinhole camera model [47].

Intrinsic Camera Parameters The camera's internal characteristics, like its focal length, principal point, and pixel scaling factors, are collectively described by the intrinsic parameters. These are organized into the 3×3 camera intrinsic matrix, \mathbf{C}_{int} , which defines the transformation from 3D coordinates in the camera's reference frame to 2D pixel coordinates on the image plane. This matrix is defined as:

$$\mathbf{C}_{int} = \begin{bmatrix} f_x & 0 & c_x \\ 0 & f_y & c_y \\ 0 & 0 & 1 \end{bmatrix} \quad (38)$$

where f_x and f_y are the focal lengths in the x and y directions, respectively, and c_x and c_y represent half the width and height of the image plane, respectively, in order to center the image. In the pinhole camera model, they are used to ensure that the u and v coordinates are always positive.

This transforms the image coordinate system to have a domain of $[0, 2c_x]$ and $[0, 2c_y]$ for u and v , respectively, rather than $[-c_x, c_x]$ and $[-c_y, c_y]$.

Extrinsic Camera Parameters The extrinsic parameters define the camera's pose (position and orientation) within the world coordinate system. These are encapsulated in the extrinsic transformation matrix denoted as $[\mathbf{\Gamma}|\mathbf{t}]$. This matrix comprises a 3×3 rotation matrix, $\mathbf{\Gamma}$, and a 3×1 translation vector, \mathbf{t} . Its function is to convert the 3D world coordinates of an object, such as the satellite, into the camera's own coordinate system according to the following relation:

$$\mathbf{C}_{ext} = \begin{bmatrix} \mathbf{\Gamma} & \mathbf{t} \\ 0 & 1 \end{bmatrix} \quad (39)$$

The transformation from world coordinates \mathbf{X}_{world} to camera coordinates \mathbf{X}_{camera} is given by:

$$\mathbf{X}_{camera} = \mathbf{\Gamma}\mathbf{X}_{world} + \mathbf{t} \quad (40)$$

Conversion from 2D Pixel Coordinates to 3D World Coordinates Reconstructing the 3D positions of the satellite's markers from their 2D image coordinates involves several steps. Initially, the 2D pixel coordinates (u, v) detected by the CNN module are transformed into the camera's coordinate system, denoted as \mathbf{X}_{camera} . This first projection is achieved using the intrinsic camera matrix \mathbf{C}_{int} according to the following relation:

$$\mathbf{X}_{camera} = \mathbf{C}_{int}^{-1} \begin{bmatrix} u \\ v \\ 1 \end{bmatrix} \cdot \mathbf{Z}_{camera} \quad (41)$$

This step uses the point's depth, \mathbf{Z}_{camera} , and the inverse intrinsic matrix, \mathbf{C}_{int}^{-1} , to map 2D pixel coordinates into the 3D camera frame.

Transformation to World Coordinates The computed 3D camera-frame coordinates are then transformed into world coordinates using the extrinsic matrix $[\mathbf{\Gamma}|\mathbf{t}]$ according to the relation:

$$\mathbf{X}_{world} = \mathbf{\Gamma}^{-1}(\mathbf{X}_{camera} - \mathbf{t}) \quad (42)$$

Through this sequence of transformations, the 2D pixel coordinates detected by the CNN are converted into 3D world coordinates. These resulting 3D points serve as the crucial measurements provided to the filter, needed for accurate estimation of the satellite's relative position and orientation.

Measurement Equations

The twelve components that make up the state vector can be separated into four sections. Each section, which is made up of three components, describes one aspect of the pose of the target satellite, ENVISAT.

$$\mathbf{x} = \underbrace{(x, y, z)}_{\text{Pos.}}, \underbrace{(\dot{x}, \dot{y}, \dot{z})}_{\text{Vel.}}, \underbrace{(p_1, p_2, p_3)}_{\text{MRP}}, \underbrace{(w_x, w_y, w_z)}_{\text{Ang. Vel.}} \quad (43)$$

It should be noted that the complete simulation uses 18 states for the propagation of absolute states, such as the position and velocity of the chaser's orbit with respect to the ECI frame. The relative position of the target and chaser's centers of mass, the center of mass's relative velocity, MRPs, and the angular velocities are the four main elements that need to be monitored.

In order to compare the predicted measurements with the actual measurements acquired from the camera system during the filter update stage, it is important to assess the marker locations based on the projected state. Let \mathbf{u} be the position vector of the center of mass of the chaser in relation to the center of mass of ENVISAT. Each marker's measurements are determined separately using the formula below:

$$\mathbf{z}_i = \mathbf{\Gamma}^T \mathbf{v}_i - \mathbf{u} \quad (44)$$

The target's reference frame, which is determined by the available CAD model of ENVISAT, is where the marker position vector \mathbf{v}_i is first expressed. After that, this vector is multiplied by the rotation matrix $\mathbf{\Gamma}$ to move to the chaser's reference frame. Lastly, a straightforward vector difference is used to calculate each marker's position measurement with respect to the chaser. Each vector \mathbf{z}_i represents the position measurement of a marker relative to the chaser's center of mass. This equation indicates that the measurement model couples translation and rotational states. Fig. 4 shows how the vectors are arranged in the measurement equations [48].

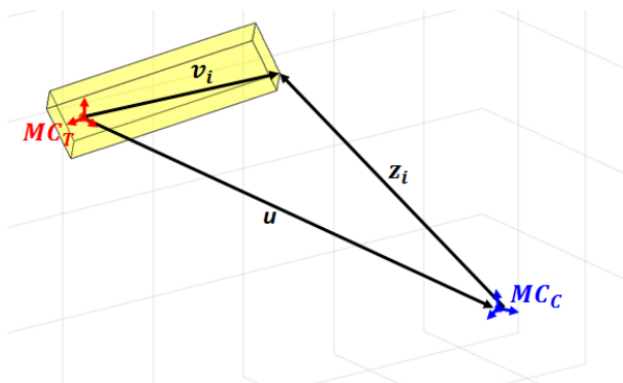


Figure 4. Arrangement of the vectors for the measurement equation

Markers Association

Following the CNN's detection of the possible marker sites, the estimated states of the filter are used to compare these measurements to the expected locations for each marker as determined by Eq. (44). By reducing the overall distance between the predicted and measured places, the association process is executed. To make sure that the anticipated marker sites are as close to the measured ones as possible, the total minimum distance is computed using the Euclidean distance. By building a cost function, J , that minimizes the squared distance between the measured marker positions, Ξ_i , and the predicted marker locations, τ_j , this procedure can be demonstrated mathematically. To properly associate each predicted marker with the closest measured marker (in a global sense), the cost function J chooses the pairings (i, j) that minimize the total squared distance:

$$J = \arg \min_{i,j} \sum_{i,j} (\Xi_i - \tau_j)^2 \quad (45)$$

Measurement Noise Covariance Calculation

To obtain a physically accurate measurement noise covariance matrix \mathbf{R} that reflects real-world sensor uncertainty, a statistical estimation procedure was developed based on repeated CNN detections over a single image. Rather than assigning arbitrary or constant values to \mathbf{R} , we empirically

derive it from repeated runs of the corner detection network under simulated variability, resulting in a data-driven characterization of 3D measurement uncertainty. The process begins with a selected image and its corresponding ground truth corner locations and depths, projected from the satellite simulation. CNN detects 2D corner positions over multiple iterations of randomized sensor perturbation. These perturbations include affine jitter, random noise injection, and controlled blur, emulating physical effects such as camera shake, sensor noise, and image degradation. Each set of detected 2D pixel positions is reprojected into 3D coordinates using the camera intrinsic matrix and the associated marker depth values. For each marker, this process yields a distribution of 3D measurements $\{\mathbf{z}_i^{(k)}\}_{k=1}^N$, where N is the number of Monte Carlo CNN runs. The sample covariance of these measurements is then computed as:

$$\mathbf{R}_i = \frac{1}{N-1} \sum_{k=1}^N (\mathbf{z}_i^{(k)} - \bar{\mathbf{z}}_i)(\mathbf{z}_i^{(k)} - \bar{\mathbf{z}}_i)^T \quad (46)$$

where $\bar{\mathbf{z}}_i$ is the mean of the 3D positions of marker i .

In order to capture a global characterization of the sensor noise model, all residuals across all markers are stacked, and a global covariance matrix \mathbf{R} is estimated:

$$\mathbf{R} = \text{cov} \left(\bigcup_i \left\{ \mathbf{z}_i^{(k)} - \bar{\mathbf{z}}_i \right\}_{k=1}^N \right) \quad (47)$$

The resulting covariance matrix is saved and integrated into the UKF initialization, ensuring the filter’s confidence in measurements reflects observed detection spread. Figure 5 visualizes the CNN-detected marker spread around the ground truth for a sample image of a parallelepiped, in order to give a visual representation of the idea, where ellipses represent 3-sigma contours of the 2D covariance.

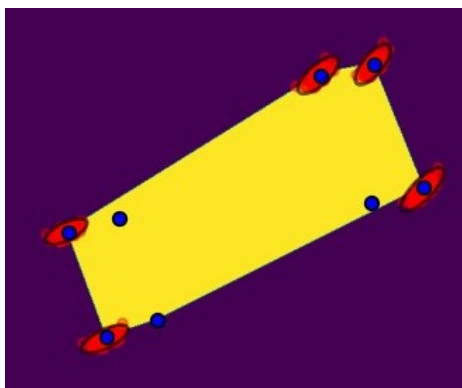


Figure 5. CNN corner detection spread under noise

Online Adaptive R-Tuning via Innovation Filtering

Beyond the process noise tuning, our work also introduces an online adaptation strategy for the measurement noise covariance matrix \mathbf{R} , which addresses a key limitation in many existing vision-based filtering pipelines: the use of static, overly conservative sensor models. Traditionally, \mathbf{R} is selected offline based on empirical measurements or hand-crafted heuristics, assuming constant

sensor quality under time and scene conditions. However, in spaceborne camera tracking, measurement uncertainty is inherently dynamic, affected by marker visibility, occlusions, blur, lighting, and external jitters. Relying on a fixed \mathbf{R} results in either overconfident updates or loss of information gain, both of which degrade filter consistency and estimation quality. In order to overcome this, we introduce a multiple tuning factor (MTF) approach, and the theoretical background behind the proposed algorithm is performing an innovation-based adaptive tuning for the measurement noise covariance matrix. Innovation in UKF structure is defined as,

$$\mathbf{e}_k = \mathbf{z}_k - \hat{\mathbf{z}}_k, \quad (48)$$

where \mathbf{e}_k is the measurement innovation. If there exist mismatches between the process and measurement models, due to the unaccounted external disturbances during the gathering of measurements, the Kalman gain changes with varying innovation covariance.

For an optimally performing Kalman filter operating in steady-state, the presence of external disturbances affecting the measurements coming from the camera is indicated when the trace of the actual error covariance surpasses a theoretical value. This condition, requiring the activation of adaptive filtering, is given by:

$$\text{tr}(\mathbf{e}_k \mathbf{e}_k^T) \geq \text{tr}(\mathbf{S}_{k-1} + \mathbf{MTF}_k + \mathbf{R}), \quad (49)$$

where $\text{tr}(\cdot)$ denotes the matrix trace. Specifically, monitoring the real innovation covariance ($\mathbf{e}_k \mathbf{e}_k^T$) at the current time k allows for the detection of instantaneous variations. So from this point, at each update step, we compute:

$$\mathbf{MTF}_k = \mathbf{e}_k \mathbf{e}_k^T - \mathbf{S}_{k-1} - \mathbf{R} \quad (50)$$

Instead of using the full \mathbf{MTF}_k matrix, only its diagonal elements are considered for the adaptive covariance update. This simplification arises from the assumption that external disturbances affecting different markers are uncorrelated. Furthermore, since covariance must be non-negative for physical significance, any negative diagonal values computed in \mathbf{MTF}_k are subsequently set to zero. This positivity constraint is enforced element-wise, represented as:

$$\mathbf{MTF}_k \leftarrow \max(0, \mathbf{MTF}_k) \quad (51)$$

where the \max operation ensures all elements are non-negative. This matrix captures underestimation in \mathbf{R} . Therefore, the assumed filter's measurement covariance now becomes

$$\mathbf{S}_k = \mathbf{S}_{k-1} + \mathbf{R} + \mathbf{MTF}_k \quad (52)$$

Unlike prior works that use batch residual statistics to adjust \mathbf{R} over long windows, our formulation is fully online and adaptive, enabling efficient tuning in real-time, even under partial marker loss, degraded imagery, or sudden lighting changes. Conceptually, the filters check how much to rely on the received measurement based on its likelihood [49], and it inflates the covariance accordingly.

Online Adaptive Q-Tuning with Smoothing Approach

In our previous study [34], we addressed the problem of missing observations due to satellite eclipses by manually adjusting the process noise covariance matrix \mathbf{Q} during known periods of

complete visual occlusion due to the eclipse. This adjustment was based on prior knowledge of the eclipse interval, during which measurement updates were entirely disabled. To compensate for the increased uncertainty caused by the absence of visual measurements, the values in \mathbf{Q} were heuristically inflated, allowing the UKF to propagate broader state uncertainty. While this approach proved effective in maintaining robust estimates under eclipse conditions, it relied heavily on manual tuning and a priori knowledge of eclipse timing and duration. In contrast, the method introduced in this work leverages the UKF's native sigma point structure to compute a forward-looking cross-covariance matrix \mathbf{D}_k , allowing adaptive \mathbf{Q} updates via a closed-form expression inspired by RTS smoothing [26]. This non-iterative, real-time update requires no batch statistics or tuning windows and automatically responds to dynamic model mismatches or visibility loss (e.g., eclipse scenarios), providing robust performance with minimal computations. Compared to previous methods, our approach scales efficiently to high-dimensional state spaces and is well-suited for embedded onboard applications in vision-based space navigation. To dynamically tune the process noise covariance \mathbf{Q} at each filter step, we compute the cross-covariance matrix \mathbf{D}_k as follows:

$$\mathbf{D}_k = \sum_{i=0}^{2L} W_c^{(i)} \left(\chi_{k-1}^{(i)} - \hat{\mathbf{x}}_{k-1} \right) \left(\chi_{k|k-1}^{(i)} - \hat{\mathbf{x}}_{k|k-1} \right)^T \quad (53)$$

where $\chi_{k-1}^{(i)}$ and $\chi_{k|k-1}^{(i)}$ denote the sigma points before and after propagation through the dynamic model, and $W_c^{(i)}$ are the unscented transform weights. This matrix captures how perturbations at time $k-1$ influence the predicted state at time k . During intervals with no measurements (e.g., eclipse), we avoid the inversion of the predicted covariance matrix $\mathbf{P}_{k|k-1}$ to compute the classical smoother gain $\mathbf{G}_k = \mathbf{D}_k (\mathbf{P}_{k|k-1})^{-1}$, which can become unstable or singular in such periods. Instead, we directly incorporate the cross-covariance into the covariance update via:

$$\mathbf{Q}_{\text{adaptive},k} = \mathbf{D}_k (\mathbf{P}_{k|k-1} - \mathbf{P}_k^-) \mathbf{D}_k^T \quad (54)$$

$$\mathbf{P}_k = \mathbf{P}_{k|k-1} + \mathbf{Q}_{\text{adaptive},k} \quad (55)$$

The analogy with the UKF-RTS smoother is evident, considering that the equations revert to the classic smoother updated with the inclusion of the state covariance inversion. This formulation preserves symmetry and positive semi-definiteness without requiring explicit matrix inversion, thus enhancing numerical robustness. Moreover, it maintains a smoothing-like behavior while avoiding the computational overhead of full RTS backward passes. As a result, the proposed method provides a lightweight and stable alternative for real-time applications under partial observability.

RESULTS

To initialize the estimation framework, uncertainty is modeled by adding zero-mean Gaussian noise to the initial state vector. The standard deviations applied to each component reflect assumed initial confidence levels, as specified in Table 2. A normal distribution with a standard deviation of $1.0m$ for position components, $1.0 \times 10^{-1}m/s$ for velocity, $1.0 \times 10^{-2}rad$ for MRPs, and $1.0 \times 10^{-3}rad/s$ for angular velocity.

Table 2. Initial conditions

Translational Dynamics		Rotational Dynamics	
x (m)	-0.002	ϕ (roll,rad)	1.66
y (m)	-31.17	θ (pitch,rad)	2.27
z (m)	0	ψ (yaw,rad)	-0.38
\dot{x} (m/s)	-3.5e-6	ω_x (rad/s)	0.02
\dot{y} (m/s)	-2.0e-6	ω_y (rad/s)	0.02
\dot{z} (m/s)	0	ω_z (rad/s)	0.04

Online Adaptive R-Tuning Results

The adaptive R-tuning enhances the estimation quality of the UKF, allowing it to trust high-confidence measurements while guarding against noisy or spurious detections. As demonstrated in Monte Carlo analysis during no eclipse scenario, the adaptive filter maintains tighter error bounds and more accurate pose estimation than the no-adaptation case for both scenarios with time-varying measurement noise. Fig. 6 shows the RMSE for translational and rotational states as follows.

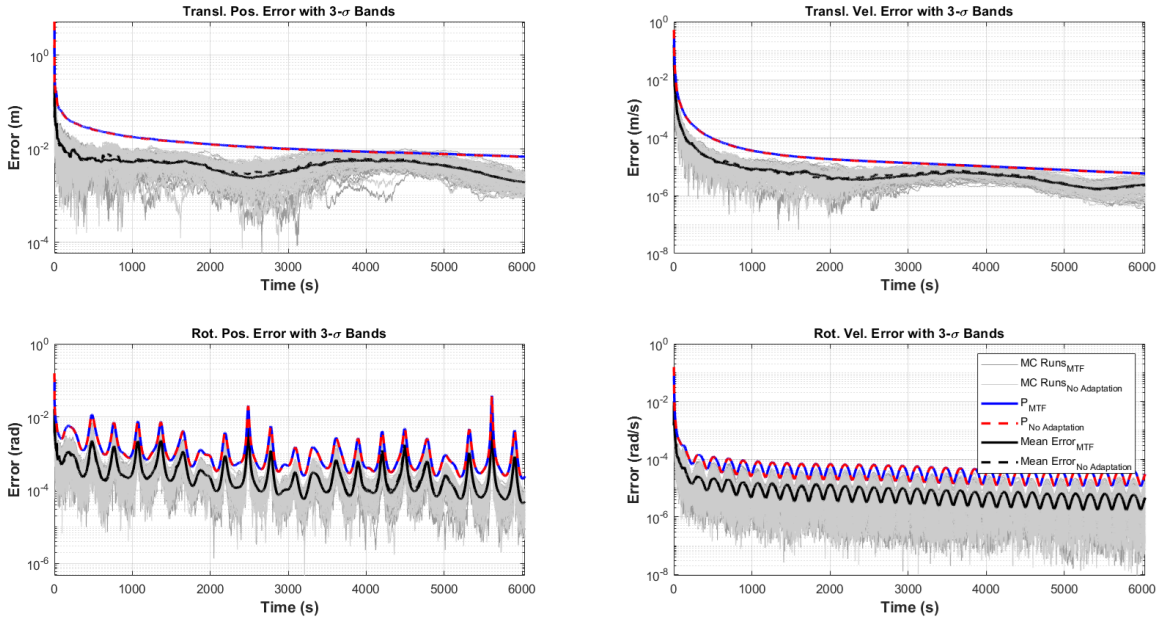


Figure 6. RMSE comparison for MTF and no adaptation cases for the no-eclipse scenario

Moreover, in order to assess filter consistency, our work adopts the Scaled Normalized Estimation Error Squared (SNEES) metric, a commonly used statistical indicator that evaluates the alignment between the predicted uncertainty and the actual estimation error. As formulated and shown in [50], SNEES compares the squared estimation error with the predicted covariance matrix across Monte Carlo trials. A SNEES value close to one indicates a statistically consistent filter, while significant deviations suggest overconfidence ($SNEES > 1$) or excessive conservatism ($SNEES < 1$).

$$SNEES(k) = \frac{1}{N_s N_m} \sum_{j=1}^{N_m} (\mathbf{x}_{k,j} - \hat{\mathbf{x}}_{k|k,j})^T \mathbf{P}_{k|k,j}^{-1} (\mathbf{x}_{k,j} - \hat{\mathbf{x}}_{k|k,j}) \quad (56)$$

Here, $\mathbf{x}_{k,j}$ represents the true state vector at time step k for the j -th Monte Carlo run, and $\hat{\mathbf{x}}_{k|k,j}$ denotes the corresponding filter estimate. The term $\mathbf{P}_{k|k,j}$ is the estimated error covariance matrix by UKF. The constants N_s and N_m refer to the state dimension and the total number of Monte Carlo runs (e.g., $N_m = 100$), respectively. We compute SNEES using the predicted covariance and the Monte Carlo sample errors, leveraging our existing filter outputs without introducing additional simulation overhead. This approach allows us to quantify how well the filter captures the true uncertainty during conditions of measurement degradation, such as eclipses or marker dropout, and further substantiates the robustness of our dual-adaptive framework. So, to evaluate the consistency of the proposed R-adaptive UKF using the MTF strategy, we analyzed the SNEES over time for both the adaptive and non-adaptive cases as shown in Fig. 7.

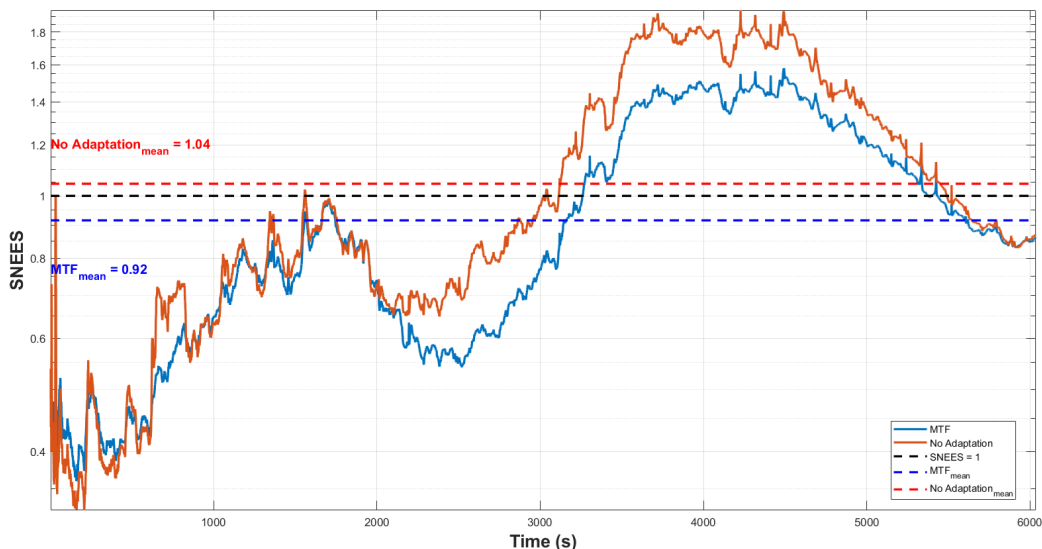


Figure 7. SNEES comparison for MTF and no adaptation cases for the no-eclipse scenario

These results demonstrate that there is no big difference between the MTF approach and a non-adaptive filter for the sake of consistency, but the MTF approach improves estimation accuracy, making it more reliable and responsive in dynamic vision-based tracking scenarios.

Online Adaptive Q-Tuning Results

The Q tuning formulation ensures that increased uncertainty due to the no-markers and no-measurement case is captured efficiently by the filter. Now, in order to evaluate the performance of this adaptation, a hundred Monte Carlo runs are executed with and without the Q adaptation for the eclipse scenario. Fig. 8 shows the root mean squared errors (RMSE) for translational and rotational states as follows. The red dashed line represents 3- σ bounds from the approach with fixed Q values, and the solid blue lines indicate the predicted 3- σ bounds from MTF + Q adaptive filter. Monte Carlo simulation errors are shown in gray where darker gray representing the adaptation Monte Carlo errors, while lighter gray represents no adaptation Monte Carlo errors. The solid black line represents the adaptive mean error, while the dashed black line represents the no adaptation mean error. For the ENVISAT satellite, the eclipse duration was calculated to be 35.57 minutes. The most notable improvement is observed during and after the eclipse interval starting at 2130th second, where the adaptive filter maintains tighter 3- σ bounds that closely track the actual error evolution.

On the other hand, the non-adaptive case shows a growing divergence between predicted covariance and actual error. Particularly in each channel, the \mathbf{Q} -adaptive method significantly reduces over-conservativeness in \mathbf{P} while simultaneously preventing underestimation of state uncertainty. These results confirm the effectiveness of our data-driven, forward-smoothed \mathbf{Q} -update strategy, which enables the UKF to retain robustness and confidence during long measurement outages. Fig. 9 presents the SNEES over time for both the proposed \mathbf{Q} -adaptive UKF and the baseline filter without \mathbf{Q} adaptation. The dashed black line denotes the ideal consistency threshold at SNEES = 1, where the filter’s predicted covariance matches the true estimation error. Figure 9 compares the filter performance between the adaptive filter and the fixed \mathbf{Q} case.

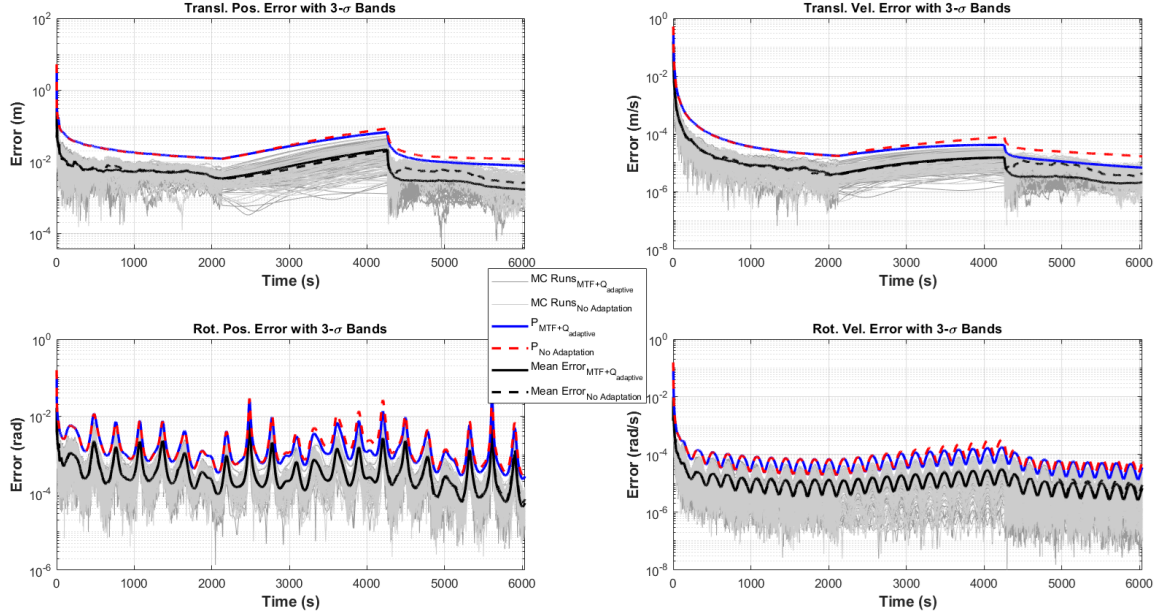


Figure 8. RMSE comparison for $\text{MTF} + \mathbf{Q}_{\text{adaptation}}$ and no adaptation cases for the eclipse scenario

The non-adaptive filter demonstrates a high average SNEES value of 0.57, indicating that the filter is significantly conservative, especially during the eclipse period. On the other hand, our adaptive filter maintains a significantly better average SNEES of 0.72, reflecting a better match between the predicted covariance and the actual estimation errors. Although still slightly conservative compared to the ideal threshold, the adaptive case shows improved consistency and resilience, particularly during the eclipse period when measurements are fully absent. The filter achieves this by leveraging a data-driven correction term that inflates \mathbf{Q} proportionally to state divergence, eliminating the need for manually scheduled noise profiles. This result demonstrates that cross-covariance-based \mathbf{Q} -tuning successfully mitigates overconfidence, yielding improved consistency while preserving estimation performance even under complete observability loss. To comprehensively evaluate the impact of the proposed dual adaptation strategy, Table 3 presents a detailed comparison of RMSE values for all 12 states under both Eclipse (E) and No Eclipse (NE) conditions. The results are computed across multiple Monte Carlo simulations and are reported for different filter configurations. UKF with no adaptation, MTF tuning only, and the proposed fully adaptive filter with simultaneous $\mathbf{Q}_{\text{adaptive}}$ and MTF tuning.

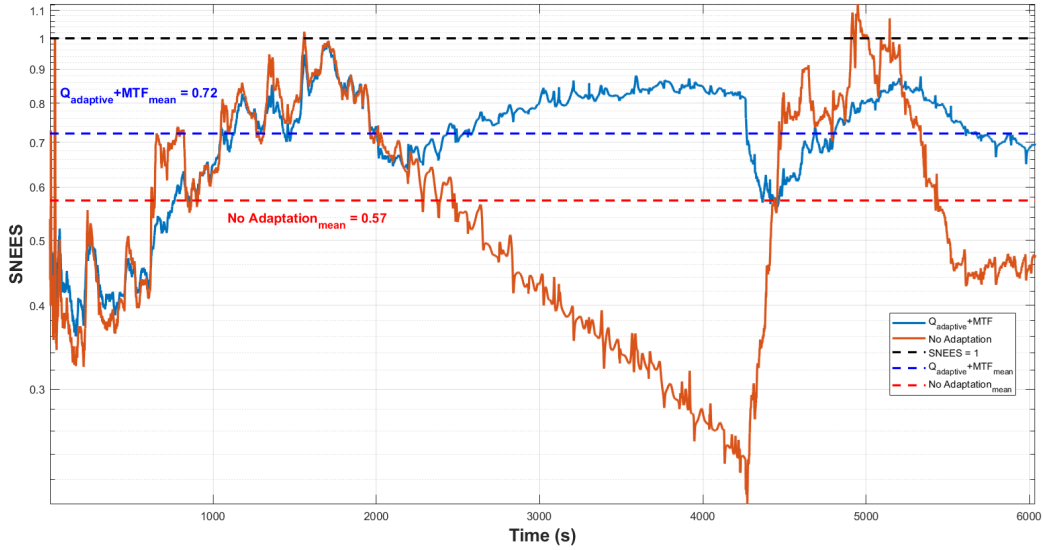


Figure 9. SNEES comparison for MTF + $Q_{adaptation}$ and no adaptation cases for the eclipse scenario

Table 3. RMSE values under Eclipse (E) and No Eclipse (NE) conditions for different methods

State	Method	RMSE (E / NE)	State	Method	RMSE (E / NE)
x	MTF + $Q_{adaptive}$	0.00310 /– m	p_1	MTF + $Q_{adaptive}$	1.592×10^{-4} /– rad
	MTF	0.00370/0.00240 m		MTF	$1.541 \times 10^{-4}/1.309 \times 10^{-4}$ rad
	No Adaptation	0.00390/0.00250 m		No Adaptation	$1.582 \times 10^{-4}/1.387 \times 10^{-4}$ rad
y	MTF + $Q_{adaptive}$	0.00250 /– m	p_2	MTF + $Q_{adaptive}$	1.749×10^{-4} /– rad
	MTF	0.00260/0.00230		MTF	$1.710 \times 10^{-4}/1.456 \times 10^{-4}$
	No Adaptation	0.00270/0.00230 m		No Adaptation	$1.744 \times 10^{-4}/1.521 \times 10^{-4}$ rad
z	MTF + $Q_{adaptive}$	0.00140 /– m	p_3	MTF + $Q_{adaptive}$	1.593×10^{-4} /– rad
	MTF	0.00140/0.00120 m		MTF	$1.545 \times 10^{-4}/1.343 \times 10^{-4}$ rad
	No Adaptation	0.00160/0.00160 m		No Adaptation	$1.533 \times 10^{-4}/1.386 \times 10^{-4}$ rad
\dot{x}	MTF + $Q_{adaptive}$	8.542×10^{-6} /– m/s	ω_x	MTF + $Q_{adaptive}$	2.639×10^{-6} /– rad/s
	MTF	$9.123 \times 10^{-6}/7.714 \times 10^{-6}$ m/s		MTF	$2.719 \times 10^{-6}/1.908 \times 10^{-6}$ rad/s
	No Adaptation	$8.631 \times 10^{-6}/7.080 \times 10^{-6}$ m/s		No Adaptation	$2.802 \times 10^{-6}/1.987 \times 10^{-6}$ rad/s
\dot{y}	MTF + $Q_{adaptive}$	5.353×10^{-6} /– m/s	ω_y	MTF + $Q_{adaptive}$	4.254×10^{-6} /– rad/s
	MTF	$6.420 \times 10^{-6}/4.665 \times 10^{-6}$ m/s		MTF	$4.389 \times 10^{-6}/3.002 \times 10^{-6}$ rad/s
	No Adaptation	$6.609 \times 10^{-6}/4.616 \times 10^{-6}$ m/s		No Adaptation	$4.623 \times 10^{-6}/3.222 \times 10^{-6}$ rad/s
\dot{z}	MTF + $Q_{adaptive}$	5.941×10^{-6} /– m/s	ω_z	MTF + $Q_{adaptive}$	2.669×10^{-6} /– rad/s
	MTF	$5.945 \times 10^{-6}/5.912 \times 10^{-6}$ m/s		MTF	$2.749 \times 10^{-6}/1.969 \times 10^{-6}$ rad/s
	No Adaptation	$7.204 \times 10^{-6}/7.165 \times 10^{-6}$ m/s		No Adaptation	$2.820 \times 10^{-6}/2.034 \times 10^{-6}$ rad/s

The results presented in Table 3 show the superior performance of the proposed dual adaptive UKF framework in both eclipse and nominal lighting conditions. In particular, the full MTF+ $Q_{adaptive}$ framework achieves the lowest RMSE in almost every state. However, RMSE can be disproportionately influenced by rare high-error transients, especially at the beginning, making it a potentially deceptive metric in highly dynamic scenarios. So, it is worth noting that the “No Adaptation” UKF

case relies on a manually fine-tuned process noise covariance matrix \mathbf{Q} . While effective in simulation, this configuration assumes prior knowledge of the system’s noise characteristics. In contrast, the adaptive MTF+ $\mathbf{Q}_{\text{adaptive}}$ approach dynamically adjusts \mathbf{Q} online, ensuring reliable performance even under conditions of intermittent marker visibility, external disturbances, or camera degradation. These enhancements come without sacrificing filter stability, making the dual adaptive UKF particularly suitable for autonomous, robust spaceborne navigation.

CONCLUSIONS

This work presents a robust and dynamically adaptive UKF framework tailored for vision-based relative navigation under challenging conditions such as intermittent marker visibility and eclipses. By leveraging MTF and innovation statistics, we propose a dual adaptation strategy that adjusts both the process noise covariance \mathbf{Q} and the measurement noise covariance \mathbf{R} in response to observed filter behavior. Our adaptation of \mathbf{R} is guided by a residual-consistency formulation that filters out non-Gaussian measurement deviations. In contrast, the adjustment of \mathbf{Q} is driven by state divergence metrics during occlusion periods, inspired by forward prediction mismatch and smoothed uncertainty propagation. Results demonstrate that our method significantly improves estimation accuracy, compared to static-filter configurations and prior techniques. Together, they yield significant reductions in estimation error across all 12 state variables compared to non-adaptive filters, and consistently lower SNEES values, particularly during challenging eclipse phases. Notably, we outperform recent neural-filter-based efforts such as the approach in [34], especially in eclipse phases where marker observations are sparse or fully absent. Our filter maintains stability and bounded covariance even during complete visual dropout, while previous approaches suffer from overly confident covariances and larger, fluctuating mean errors. Furthermore, these methods require no manual tuning and generalize across dynamic lighting and visibility conditions, positioning them as practical candidates for onboard deployment.

Future work will focus on enhancing the synergy between the estimation filter and the vision pipeline, enabling tighter closed-loop coordination where the filter dynamically guides camera focus or processing based on marker prediction confidence and visibility. In parallel, we will expand our simulation framework with LIDAR implementation in Blender, allowing for a more robust and realistic UKF measurement model that incorporates depth estimation, ultimately improving accuracy and resilience under degraded visual conditions.

REFERENCES

- [1] S. Estable, C. Pruvost, E. Ferreira, J. Telaar, M. Fruhnert, C. Imhof, T. Rybus, G. Peckover, R. Lucas, R. Ahmed, T. Oki, M. Wygachiewicz, P. Kicman, A. Lukasik, N. Santos, T. Milhano, P. Arroz, R. Biesbroek, and A. Wolahan, “Capturing and deorbiting envisat with an airbus spacetug. results from the esa e.deorbit consolidation phase study,” *Journal of Space Safety Engineering*, vol. 7, no. 1, pp. 52–66, 2020. DOI:<https://doi.org/10.1016/j.jsse.2020.01.003>.
- [2] E. A. Pensado, L. M. G. de Santos, H. G. Jorge, and M. Sanjurjo-Rivo, “Deep learning-based target pose estimation using lidar measurements in active debris removal operations,” *IEEE Transactions on Aerospace and Electronic Systems*, vol. 59, no. 5, pp. 5658–5670, 2023. DOI:[10.1109/TAES.2023.3262505](https://doi.org/10.1109/TAES.2023.3262505).
- [3] S. Jaekel, R. Lampariello, W. Rackl, M. De Stefano, N. Oumer, A. M. Giordano, O. Porges, M. Pietras, B. Brunner, J. Ratti, Q. Muehlbauer, M. Thiel, S. Estable, R. Biesbroek, and A. Albu-Schaeffer, “Design and operational elements of the robotic subsystem for the e.deorbit debris removal mission,” *Frontiers in Robotics and AI*, vol. Volume 5 - 2018, 2018. DOI:[10.3389/frobt.2018.00100](https://doi.org/10.3389/frobt.2018.00100).
- [4] S. Servadio, N. Simha, D. Gusmini, D. Jang, T. St. Francis, A. D’Ambrosio, G. Lavezzi, and R. Linares, “Risk index for the optimal ranking of active debris removal targets,” *Journal of Spacecraft and Rockets*, vol. 61, no. 2, pp. 407–420, 2024. DOI:<https://doi.org/10.2514/1.A35752>.

- [5] S. Servadio, D. Jang, and R. Linares, "Threat level estimation from possible break-up events in leo," in *AIAA SCITECH 2024 Forum*, p. 1065, 2024.
- [6] G. Lentaris, K. Maragos, I. Stratakos, L. Papadopoulos, O. Papanikolaou, D. Soudris, M. Lourakis, X. Zabulis, D. Gonzalez-Arjona, and G. Furano, "High-performance embedded computing in space: Evaluation of platforms for vision-based navigation," *Journal of Aerospace Information Systems*, vol. 15, no. 4, pp. 178–192, 2018. DOI:10.2514/1.I010555.
- [7] S. S. Rizzuto, R. Cipollone, A. De Vittori, *et al.*, "Object detection on space-based optical images leveraging machine learning techniques," *Neural Computing and Applications*, 2025. DOI:https://doi.org/10.1007/s00521-025-11069-w.
- [8] G. Furano, G. Meoni, A. Dunne, D. Moloney, V. Ferlet-Cavrois, A. Tavoularis, J. Byrne, L. Buckley, M. Psarakis, K.-O. Voss, and L. Fanucci, "Towards the use of artificial intelligence on the edge in space systems: Challenges and opportunities," *IEEE Aerospace and Electronic Systems Magazine*, vol. 35, no. 12, pp. 44–56, 2020. DOI:10.1109/MAES.2020.3008468.
- [9] L. Renaut, H. Frei, and A. Nüchter, "Deep learning on 3d point clouds for fast pose estimation during satellite rendezvous," *Acta Astronautica*, vol. 232, pp. 231–243, 2025. DOI:https://doi.org/10.1016/j.actaastro.2025.03.009.
- [10] H. Zhou, L. Yao, H. She, and W. Si, "Sdpenet: A lightweight spacecraft pose estimation network with discrete euler angle probability distribution," *IEEE Robotics and Automation Letters*, vol. 10, no. 4, pp. 3086–3093, 2025. DOI:10.1109/LRA.2025.3540379.
- [11] M. Bechini, G. Gu, P. Lunghi, and M. Lavagna, "Robust spacecraft relative pose estimation via cnn-aided line segments detection in monocular images," *Acta Astronautica*, vol. 215, pp. 20–43, 2024. DOI:https://doi.org/10.1016/j.actaastro.2023.11.049.
- [12] T. O. Dixon, S. A. Giles, and A. A. Gorodetsky, "Predicting uncertainty in vision-based satellite pose estimation using deep evidential regression," *Aerospace Science and Technology*, vol. 160, p. 110055, 2025. DOI:https://doi.org/10.1016/j.ast.2025.110055.
- [13] H. Gao, Z. Li, N. Wang, J. Yang, and D. Dang, "Su-net: pose estimation network for non-cooperative spacecraft on-orbit," *Scientific Reports*, vol. 13, p. 11780, Jul 2023. DOI:10.1038/s41598-023-38974-1.
- [14] Y. Wei, X. Yang, X. Bai, and Z. Xu, "Adaptive hybrid kalman filter for attitude motion parameters estimation of space non-cooperative tumbling target," *Aerospace Science and Technology*, vol. 144, p. 108832, 2024. DOI:https://doi.org/10.1016/j.ast.2023.108832.
- [15] R. Opromolla and A. Nocerino, "Uncooperative spacecraft relative navigation with lidar-based unscented kalman filter," *IEEE Access*, vol. 7, pp. 180012–180026, 2019. DOI:10.1109/ACCESS.2019.2959438.
- [16] S. Servadio, F. Cavenago, P. Di Lizia, and M. Massari, "Nonlinear prediction in marker-based spacecraft pose estimation with polynomial transition maps," *Journal of Spacecraft and Rockets*, vol. 59, no. 2, pp. 511–523, 2022. DOI:10.2514/1.A35068.
- [17] Y. Wang, S. Sun, and L. Li, "Adaptively robust unscented kalman filter for tracking a maneuvering vehicle," *Journal of Guidance, Control, and Dynamics*, vol. 37, no. 5, pp. 1696–1701, 2014. DOI:10.2514/1.G000257.
- [18] S. Servadio and R. Zanetti, "Recursive polynomial minimum mean-square error estimation with applications to orbit determination," *Journal of Guidance, Control, and Dynamics*, vol. 43, no. 5, pp. 939–954, 2020. DOI:https://doi.org/10.2514/1.G004544.
- [19] S. Servadio, R. Zanetti, and B. A. Jones, "Nonlinear filtering with a polynomial series of gaussian random variables," *IEEE Transactions on Aerospace and Electronic Systems*, vol. 57, no. 1, pp. 647–658, 2020. DOI:10.1109/TAES.2020.3028487.
- [20] M. Driedger, M. Rososhansky, and P. Ferguson, "Unscented Kalman filter-based method for spacecraft navigation using resident space objects," *CEAS Space Journal*, vol. 3, 2020. DOI:https://doi.org/10.1007/s42401-020-00055-w.
- [21] D. Kaidanovic, M. Piazza, M. Maestrini, and P. Di Lizia, "Deep learning-based relative navigation about uncooperative space objects," in *73rd International Astronautical Congress*, 09 2022. EID:2-s2.0-85167571157.
- [22] S. Sampath and J. Feng, "Neural network-based synchronisation of free-floating space manipulator's joint motion and mother spacecraft's attitude for active debris removal," in *2024 IEEE Congress on Evolutionary Computation (CEC)*, pp. 1–10, 2024. DOI:10.1109/CEC60901.2024.10611860.
- [23] R. Mamich and R. Zanetti, "Applying Correlation Methods to Relative Navigation," in *AAS/AIAA Astrodynamics Specialist Conference*, (Broomfield, CO), August 2024. Conference held August 11-15.
- [24] R. Moghe, R. Zanetti, and M. R. Akella, "Adaptive kalman filter for detectable linear time-invariant systems," *Journal of Guidance, Control, and Dynamics*, vol. 42, no. 10, pp. 2197–2205, 2019. DOI:10.2514/1.G004359.

- [25] R. Zanetti and C. N. D'Souza, "Observability analysis and filter design for the orion earth-moon attitude filter," *Journal of Guidance, Control, and Dynamics*, vol. 39, no. 2, pp. 201–213, 2016. DOI:10.2514/1.G001217.
- [26] S. Särkkä, *Bayesian Filtering and Smoothing*. Cambridge University Press, 2013.
- [27] B. Candan and H. E. Soken, "Robust attitude estimation using imu-only measurements," *IEEE Transactions on Instrumentation and Measurement*, vol. 70, pp. 1–9, 2021. DOI:10.1109/TIM.2021.3104042.
- [28] B. Candan and H. E. Soken, "Robust attitude estimation using magnetic and inertial sensors," *IFAC-PapersOnLine*, vol. 56, no. 2, pp. 4502–4507, 2023. DOI:https://doi.org/10.1016/j.ifacol.2023.10.941.
- [29] H. E. Soken and C. Hajiyev, "Ukf-based reconfigurable attitude parameters estimation and magnetometer calibration," *IEEE Transactions on Aerospace and Electronic Systems*, vol. 48, no. 3, pp. 2614–2627, 2012. DOI:10.1109/TAES.2012.6237612.
- [30] N. Simha, S. Servadio, M. Lifson, G. Lavezzi, and R. Linares, "Optimal active debris removal mission planning to inform policy decisions," *Acta Astronautica*, vol. 228, pp. 224–236, 2025. DOI:https://doi.org/10.1016/j.actaastro.2024.11.050.
- [31] D. Jang, D. Gusmini, P. M. Siew, A. D'Ambrosio, S. Servadio, P. Machuca, and R. Linares, "New monte carlo model for the space environment," *Journal of Spacecraft and Rockets*, pp. 1–22, 2025. DOI:https://doi.org/10.2514/1.A36137.
- [32] European Space Agency, ed., *Envisat Mission: Opportunities for Science and Applications*, vol. 1218 of *EŠA SP*, (Noordwijk, The Netherlands), European Space Agency, Jan. 1998.
- [33] P. Di Lizia, M. Massari, F. Cavenago, and A. Wittig, "Assessment of onboard DA state estimation for spacecraft relative navigation," Final Report ACT-RPT-MAD-ARI-16-5201, European Space Agency (ESA), Advanced Concepts Team (ACT), June 2017. Ariadna Study 16/5201. Contract IPL-PTE/LF/as/517.2016.
- [34] B. Candan and S. Servadio, "Markers identification for relative pose estimation of an uncooperative target," in *AAS/AIAA Astrodynamics Specialist Conference*, (Broomfield, CO), August 2024. DOI:10.48550/arXiv.2407.20515.
- [35] B. Candan and S. Servadio, "Relative pose estimation of an uncooperative target with camera marker detection," *Aerospace*, vol. 12, no. 5, 2025. DOI:10.3390/aerospace12050425.
- [36] A. Krizhevsky, I. Sutskever, and G. E. Hinton, "Imagenet classification with deep convolutional neural networks," in *Advances in Neural Information Processing Systems* (F. Pereira, C. Burges, L. Bottou, and K. Weinberger, eds.), vol. 25, Curran Associates, Inc., 2012. DOI:https://doi.org/10.1145/3065386.
- [37] J. Wang, K. Sun, T. Cheng, B. Jiang, C. Deng, Y. Zhao, D. Liu, Y. Mu, M. Tan, X. Wang, W. Liu, and B. Xiao, "Deep high-resolution representation learning for visual recognition," *IEEE Transactions on Pattern Analysis and Machine Intelligence*, vol. 43, no. 10, pp. 3349–3364, 2021. DOI:10.1109/TPAMI.2020.2983686.
- [38] L. Alzubaidi, J. Zhang, A. J. Humaidi, A. Q. Al-Dujaili, Y. Duan, O. Al-Shamma, J. Santamaría, M. A. Fadhel, M. Al-Amidie, and L. Farhan, "Review of deep learning: concepts, CNN architectures, challenges, applications, future directions," *Journal of big data*, vol. 8, 3 2021. DOI:10.1186/s40537-021-00444-8.
- [39] Y. Zhou, H. Qi, and Y. Ma, "End-to-end wireframe parsing," in *2019 IEEE/CVF International Conference on Computer Vision (ICCV)*, pp. 962–971, 2019. DOI:10.1109/ICCV.2019.00105.
- [40] F. Cavenago, P. Di Lizia, M. Massari, S. Servadio, and A. Wittig, "Da-based nonlinear filters for spacecraft relative state estimation," in *2018 Space Flight Mechanics Meeting*, 01 2018. DOI:10.2514/6.2018-1964.
- [41] L. Pasqualetto Cassinis, R. Fonod, and E. Gill, "Review of the robustness and applicability of monocular pose estimation systems for relative navigation with an uncooperative spacecraft," *Progress in Aerospace Sciences*, vol. 110, p. 100548, 2019. DOI:https://doi.org/10.1016/j.paerosci.2019.05.008.
- [42] L. Pauly, W. Rharbaoui, C. Shneider, A. Rathinam, V. Gaudillière, and D. Aouada, "A survey on deep learning-based monocular spacecraft pose estimation: Current state, limitations and prospects," *Acta Astronautica*, vol. 212, pp. 339–360, 2023. DOI:https://doi.org/10.1016/j.actaastro.2023.08.001.
- [43] J. Chen, L.-h. Zou, J. Zhang, and L. Dou, "The comparison and application of corner detection algorithms," *Journal of Multimedia*, vol. 4, pp. 435–441, 12 2009. DOI:10.4304/jmm.4.6.435-441.
- [44] H. Wang and M. Brady, "Real-time corner detection algorithm for motion estimation," *Image and vision computing*, vol. 13, pp. 695–703, 11 1995. DOI:10.1016/0262-8856(95)98864-p.
- [45] J. A. Noble, "Finding corners," *Image and Vision Computing*, vol. 6, no. 2, pp. 121–128, 1988. DOI:https://doi.org/10.1016/0262-8856(88)90007-8.
- [46] C. Harris and M. Stephens, "A combined corner and edge detector," in *Proceedings of the Alvey Vision Conference*, pp. 23.1–23.6, Alvey Vision Club, 1988. DOI:10.5244/C.2.23.

- [47] P. Corke, *Robotics, Vision and Control: Fundamental Algorithms in MATLAB*. Springer, 9 2011.
- [48] S. Servadio, *High Order Filters for Relative Pose Estimation of an Uncooperative Target*. PhD thesis, Politecnico di Milano, 2017.
- [49] S. Servadio, "Likelihood scouting via map inversion for a posterior-sampled particle filter," *IEEE Transactions on Aerospace and Electronic Systems*, 2024. DOI:10.1109/TAES.2024.3446757.
- [50] F. Giraldo-Gruoso, A. A. Popov, U. D. Hanebeck, and R. Zanetti, "Optimal Grid Point Sampling for Point Mass Filtering," in *AAS/AIAA Space Flight Mechanics Meeting*, (Kaua'i, HI), January 2025. Conference held January 19-23.